Journal of Medicinal Chemistry

pubs.acs.org/jmc

Article

Design, Synthesis, and Evaluation of ^{99m}Tc-Labeled Aminoadipic Acid-Urea-Lysine (AuK) as a Novel SPECT Tracer Targeting PSMA

Zuojie Li, Peiwen Han, Lina Diao, Jianyong Jiang,* and Junbo Zhang*

Cite This: https://doi.org/10.1021/acs.jmedchem.5c03275

Read Online

ACCESS | Metrics & More | Article Recommendations | Supporting Information

ABSTRACT: The high kidney uptake of prostate-specific membrane antigen (PSMA) radiotracers remains a significant challenge in the clinical diagnosis and treatment of prostate cancer (PCa). The aim of this study was to reduce the absolute kidney uptake of PSMA tracers by modifying targeting groups, thereby increasing the tumor-to-kidney (T/K) ratio. [^{99m}Tc]Tc-AuK-NapLPRO-HYNIC-EDDA demonstrated the most prominent imaging potential. It bound stably within the active cavity of the PSMA protein with nanomolar affinity (K_d = 14.73 nM). Density functional theory (DFT) and molecular dynamics provide a theoretical framework for understanding tracer coordination structures and ligand-protein interactions. [^{99m}Tc]Tc-AuK-NapLPRO-HYNIC-EDDA effectively reduced kidney uptake (1.19 ± 0.19% ID/g, 4 h) and resulted in good tumor retention, with rapid clearance from nontarget organs resulting in a high target-to-background ratios (TBRs). High-contrast SPECT/CT images were obtained within 2 to 4 h postinjection, indicating that [^{99m}Tc]Tc-AuK-NapLPRO-HYNIC-EDDA holds great potential for both standard and time-lapse imaging in PCa.

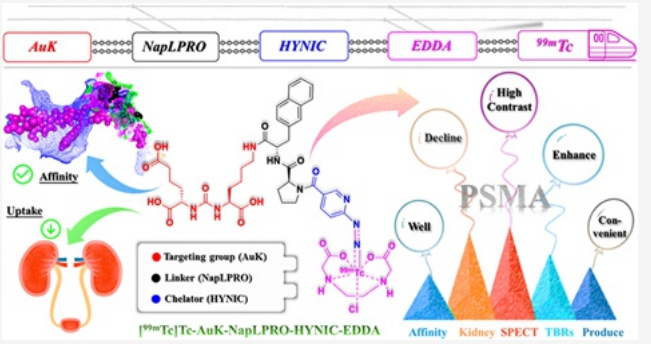

INTRODUCTION

Prostate cancer (PCa) is the most common malignancy of the male reproductive system. With its incidence and mortality rates rising globally, it constitutes a significant public health challenge.[1−3] Effective diagnosis is therefore crucial for patient treatment and prognosis. Radiotracers serve as valuable tools in the clinical diagnosis of PCa.[4−6] However, their high physiological uptake in the kidneys often leads to diagnostic interference and increased radiation doses to organs[7,8]

Prostate-specific membrane antigen (PSMA) is a critical target for developing diagnostic and therapeutic agents for PCa.[9−11] Glutamate-urea-lysine (EuK, Figure 1) has been extensively studied as a well-established scaffold for PSMA-targeting radiopharmaceuticals because of its high affinity (IC_{50} = 47 nM).[12−14] Recent studies suggest that the high uptake of EuK-based tracers in the kidneys and salivary glands may be attributed to the presence of a glutamate (Glu) moiety within the EuK pharmacophore.[15] This moiety binds within the S1' pocket of PSMA, where its carboxyl group acts as an excellent hydrogen bond acceptor, forming extensive interactions with surrounding amino acids.[16−19] These interactions are crucial for stabilizing the protein−ligand complex. Consequently, modifying the EuK scaffold presents a rational and promising strategy for optimizing PSMA-targeted radiotracers.

Herein, both PSMA137 (Glu substituted with notoginsenic acid) developed by Yang et al.[20] and the HTK03149 precursor (Glu substituted with aminoadipic acid) developed by Lin et al.[15] were designed based on this modification strategy. The modified targeting groups maintained high affinity for PSMA, and their high uptake in kidneys and salivary glands was effectively mitigated after radiolabeling.[21−23] In particular, compared with [^{177}Lu]Lu-PSMA-617, [^{177}Lu]Lu-HTK03149 demonstrated a 145% increase in tumor uptake and a 70% decrease in kidney, resulting in a 7.1-fold improvement in the tumor-to-kidney ratio. Radiotherapy studies revealed that only half the administered dose of [^{177}Lu]Lu-PSMA-617 was required for [^{177}Lu]Lu-HTK03149 to achieve comparable median survival.[15] The modification strategy for targeting groups shows substantial potential in reducing nontargeted organ uptake and represents a promising approach for further optimizing tracer performance. Initial attempts with the aminoadipic acid-urea-lysine (AuK, Figure 1) targeting group, in particular, validated its potential in addressing the challenge of high kidney uptake observed for PSMA-targeted radiotracers.

In radiotracer design, the linker between the targeting group and the radionuclide chelator plays a critical role in modulating pharmacokinetic properties. Recent studies have highlighted

Received: November 10, 2025
Revised: December 19, 2025
Accepted: December 26, 2025

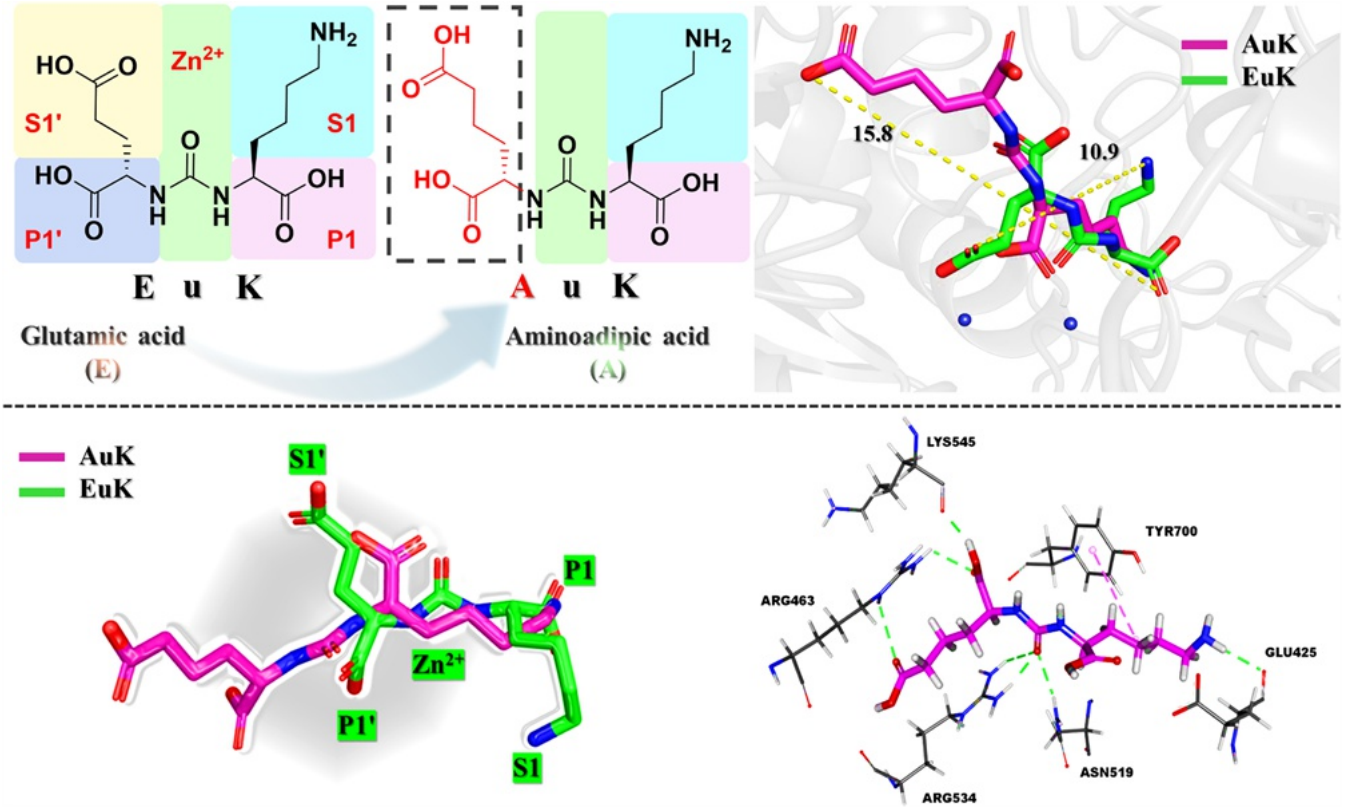

Figure 1. Molecular design (PDB: 4LQG) and structures of PSMA-targeting groups.

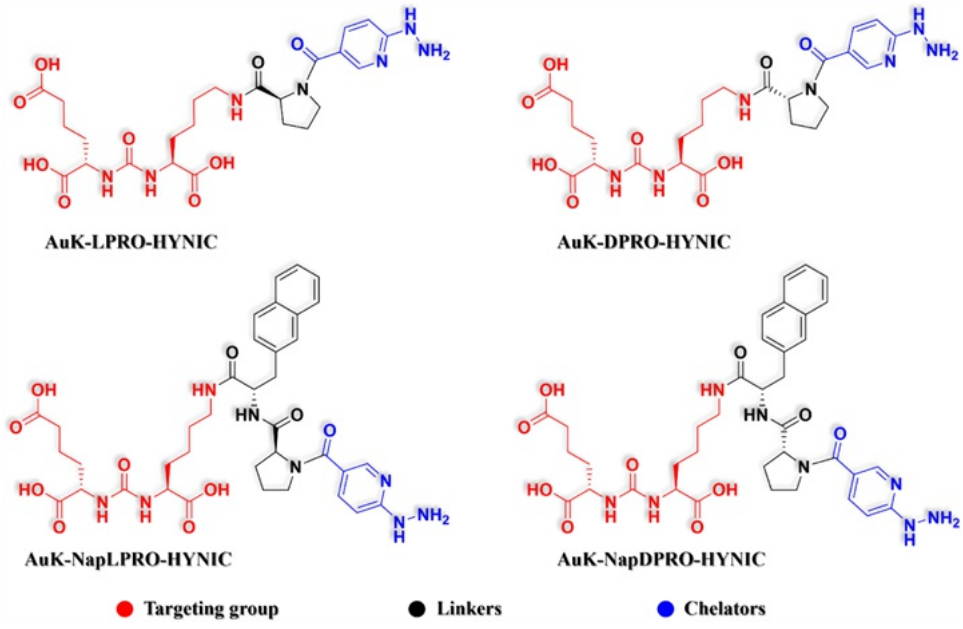

Figure 2. Molecular structures of PSMA precursors.

the potential of proline in reducing glomerular reabsorption.[24,25] Consistent with this, our previous work demonstrated that incorporating proline as a linker effectively reduces tracer uptake in nontarget organs, particularly the kidneys.[26,27] Furthermore, structural insights from PSMA617 have revealed that naphthylalanine forms a new hydrophobic pocket near the active cavity of PSMA protein, which contributes to improved pharmacokinetics and enhanced absolute tumor uptake.[28,29] With respect to ^{99m}Tc labeling, the bifunctional chelator hydrazinonicotinamide (HYNIC) can form stable complexes in the presence of coligands. The specific choice of these coligands provides a versatile strategy for fine-tuning tracer stability, lipophilicity, and target binding affinity[30]

In this study, we aimed to enhance SPECT imaging quality by modifying the PSMA-targeting group to reduce the absolute renal uptake of the tracer. To achieve this goal, we employed a rational design based on AuK as the targeting group and HYNIC as the chelator. These constructs were radiolabeled

https://doi.org/10.1021/acs.jmedchem.5c03275
J. Med. Chem. XXXX, XXX, XXX−XXX

Scheme 1. Synthetic Route of PSMA Precursors[a]

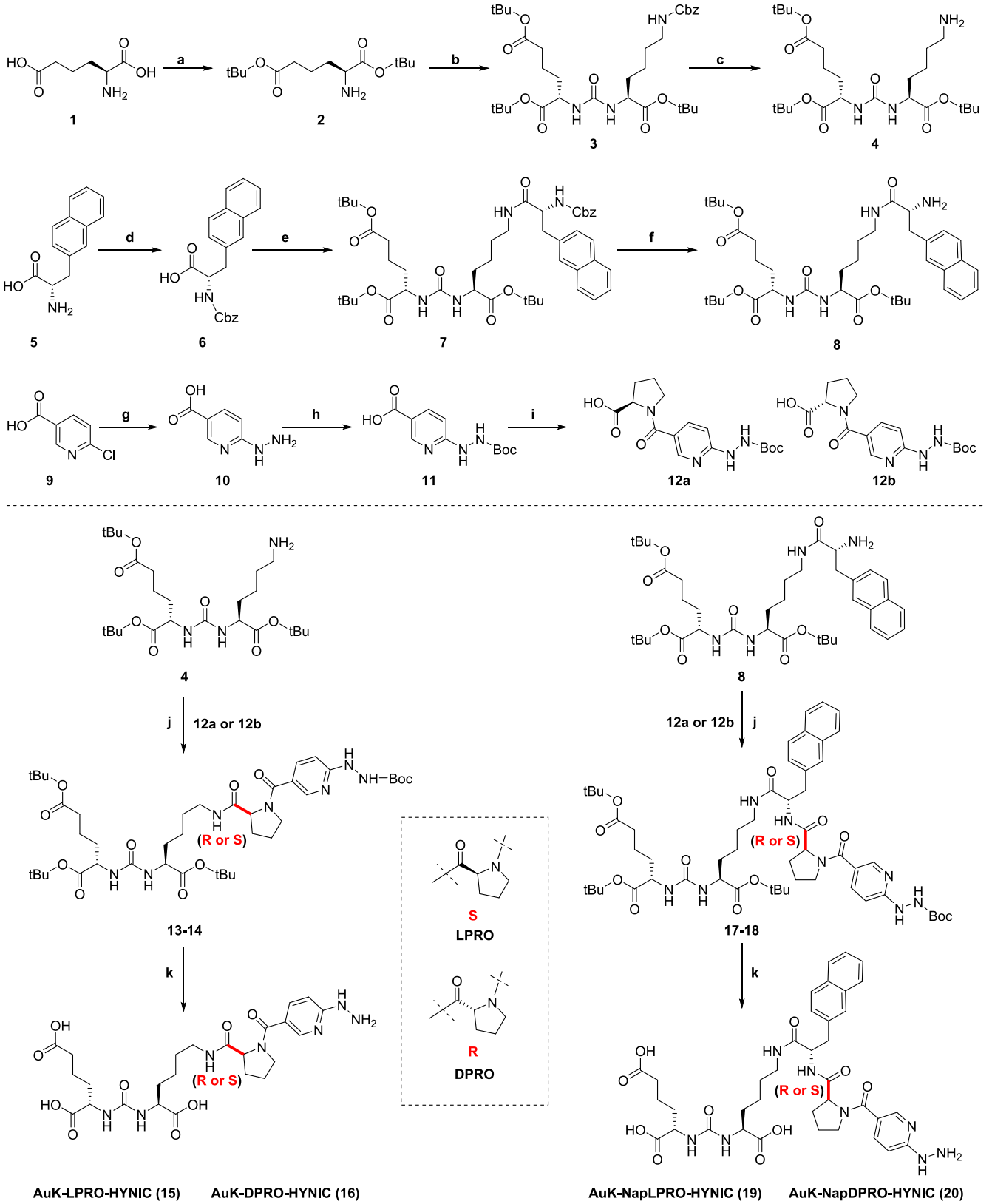

[a](a) Tert-butyl acetate, $HClO_4$, EtOH, rt; (b) Triphosgene, N-benzyloxycarbonyl-L-lysine tert-butyl ester hydrochloride, TEA, DCM, rt; (c) Pd/C, H_2, MeOH, rt; (d) Cbz-Cl, DCM, rt; (e) HATU, TEA, DMF, rt; (f) Pd/C, H_2, MeOH, rt; (g) hydrazine hydrate, H_2O,100 °C; (h) Di-*tert*-butyl dicarbonate, TEA, DMF, rt; (i) L/D-Pro, HATU, TEA, DMF, rt; (j) HATU, DIPEA, DMF, rt; and (k) TFA, DCM, rt.

with ^{99m}Tc in the presence of various coligands—triphenylphosphine trisulfonate (TPPTS), diphenylphosphine benzene-3-sulfonate (TPPMS), ethylenediaminetetraacetic acid (EDDA), and tris(hydroxymethyl)-methylglycine (tricine).

https://doi.org/10.1021/acs.jmedchem.5c03275
J. Med. Chem. XXXX, XXX, XXX−XXX

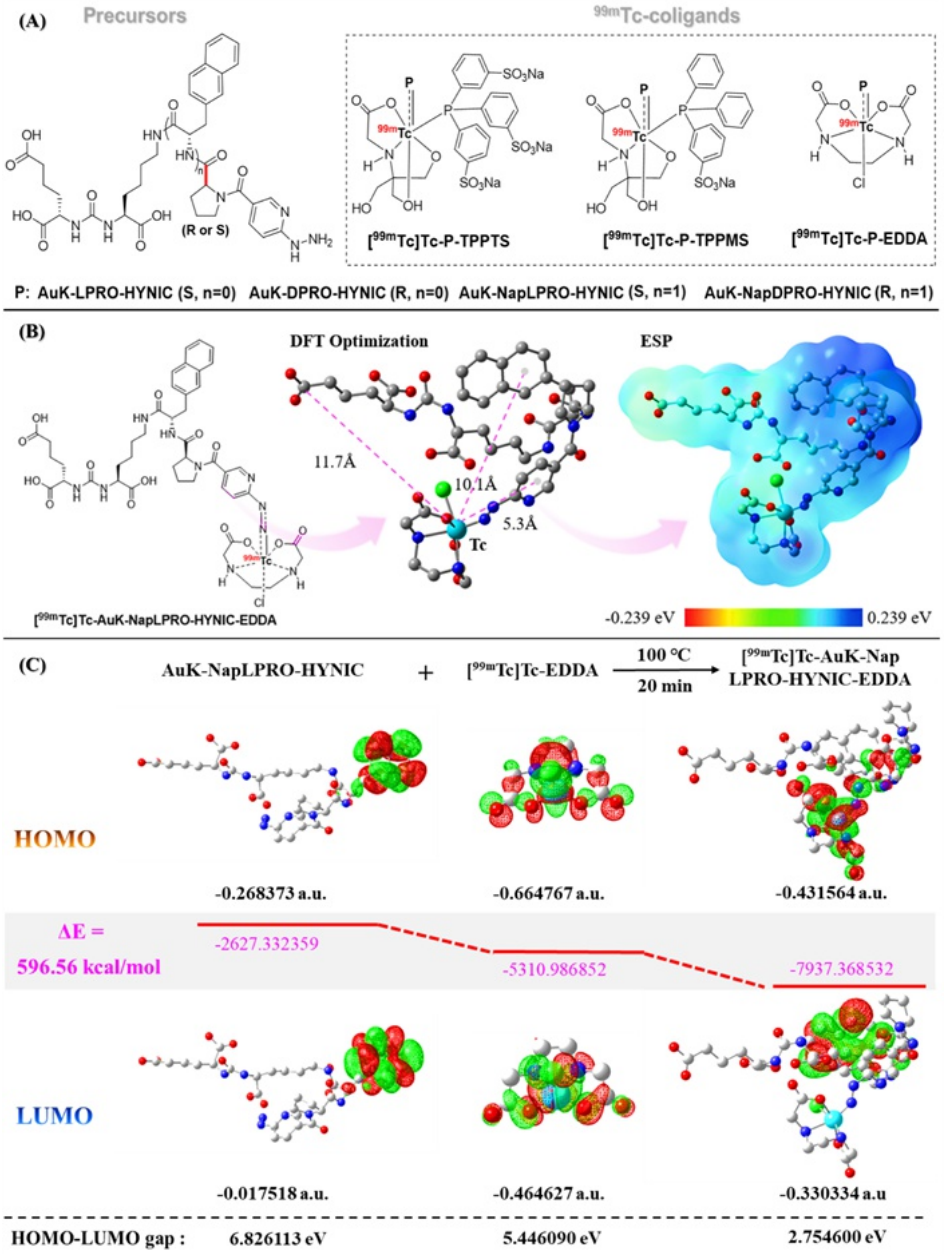

Figure 3. Speculated and DFT-calculated structures of PSMA radiotracers. (A) Speculated structure of the ^{99m}Tc-labeled compound; (B) Optimal DFT-calculated structure of [^{99m}Tc]Tc-AuK-NapLPRO-HYNIC-EDDA; and (C) Molecular orbitals of [^{99m}Tc]Tc-AuK-NapLPRO-HYNIC-EDDA.

To further optimize the tracer performance, we systematically investigated the effects of different linkers. Their pharmacokinetics and potential as SPECT imaging tracers after radiolabeling with ^{99m}Tc were evaluated *in vitro* and *in vivo*.

RESULTS

Molecular Design

The molecular docking results of the targeting groups AuK and EuK revealed distinct binding modes within the PSMA protein cavity. As shown in Figure 1, the topological distance of EuK is 10.9 Å, whereas that of AuK is 15.8 Å. Compared with that of EuK, AuK is shifted toward the exterior of the binding pocket. Specifically, the lysine moiety moves toward the Zn^{2+} domain and detaches from the S1 pocket, whereas the ureido group shifts near the P1' pocket, and the aminocaproic acid chain extends outward. Within the PSMA active site, AuK forms stable hydrogen bonds with the residues GLU425, ARG463, ASN519, ARG534, and LYS545. The molecular docking score suggests that AuK has binding affinity comparable to, or potentially more favorable than, that of EuK (−10.00 kcal/mol vs −9.40 kcal/mol). As a PSMA-targeting group, AuK was used to design four labeled precursors by varying the linkers between the targeting and chelating moieties. These precursors were AuK-LPRO-HYNIC (with L-proline), AuK-DPRO-HYNIC (with D-proline), AuK-NapLPRO-HYNIC (with naphthylalanine-L-proline), and AuK-NapDPRO-HYNIC (with naphthylalanine-D-proline), as illustrated in Figure 2.

https://doi.org/10.1021/acs.jmedchem.5c03275
J. Med. Chem. XXXX, XXX, XXX−XXX

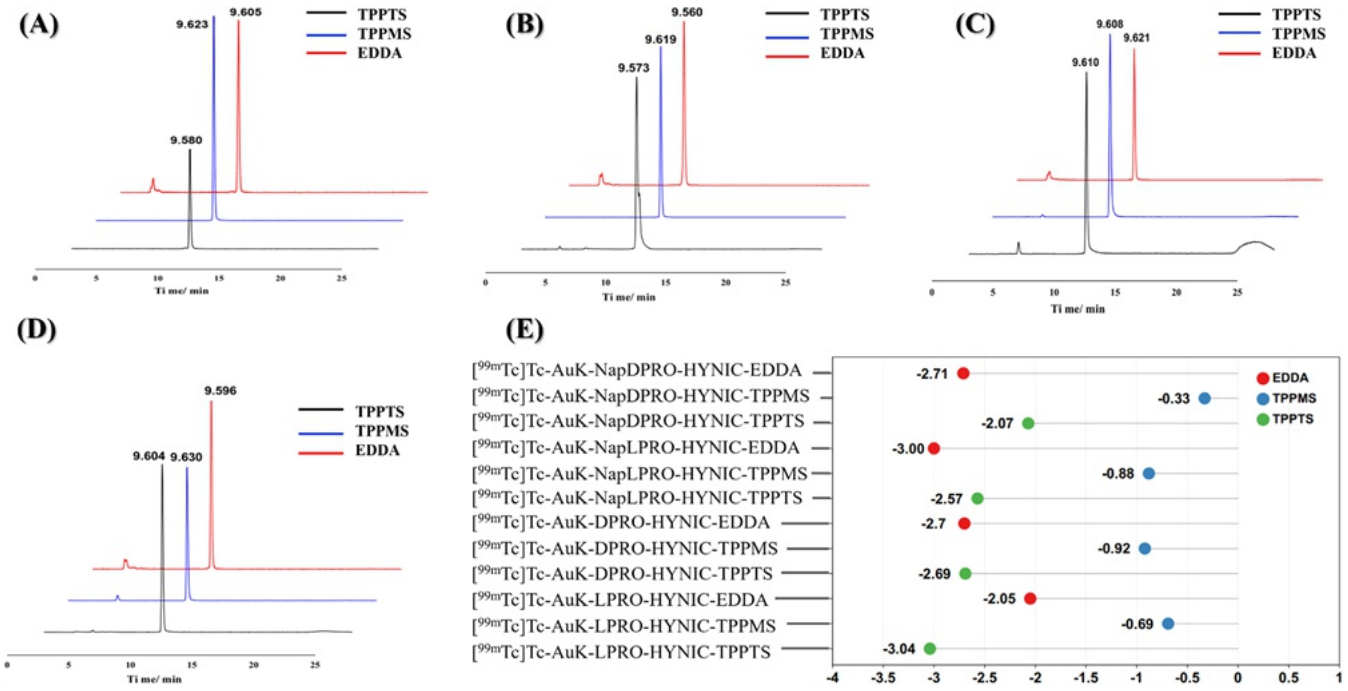

Figure 4. HPLC characterization and Log *P* of PSMA radiotracers. (A) [^{99m}Tc]Tc-AuK-LPRO-HYNIC-TPPTS/TPPMS/EDDA; (B) [^{99m}Tc]Tc-AuK-DPRO-HYNIC-TPPTS/TPPMS/EDDA; (C) [^{99m}Tc]Tc-AuK-NapLPRO-HYNIC-TPPTS/TPPMS/EDDA; (D) [^{99m}Tc]Tc-AuK-NapDPRO-HYNIC-TPPTS/TPPMS/EDDA; and (E) Log *P* of PSMA radiotracers.

Chemistry

The synthesis of the PSMA-targeting precursor is shown in Scheme 1. The targeting group AuK was synthesized starting from aminohexanedioic acid. Triphosgene was used as a carrier to react with secondary amines to form isocyanate intermediates, which then react with lysine to produce a urea moiety. In the presence of the coupling agent 2-(7-azabenzotriazol-1-yl)-*N,N,N′,N′*-tetramethyluronium hexafluorophosphate (HATU), AuK is connected to different linkers on the chelating agent through stable amide bonds. Following deprotection, four target precursors were obtained in yields of 44.75%, 53.57%, 63.01%, and 50.07%, respectively. All compounds were characterized by ^{1}H nuclear magnetic resonance (^{1}H NMR) and mass spectrometry (MS). The purity of all the precursors was greater than 95%.

Radiolabeling

As shown in Figure 3A, each precursor formed three stable ^{99m}Tc-labeled compounds with different coligands (TPPTS, TPPMS, and EDDA), yielding a total of 12 PSMA-targeting SPECT tracers. The radiolabeling procedures for all the tracers followed standardized protocols, with the entire process—from labeling to analysis—completed within 60 min. Density functional theory (DFT) optimization of the [^{99m}Tc]Tc-AuK-NapLPRO-HYNIC-EDDA structure revealed distances of 11.7 Å, 10.1 Å, and 5.3 Å from the Tc metal center to the aminohexanedioic acid group, the aromatic ring center of naphthylalanine, and the aromatic ring center of the HYNIC chelator, respectively (Figure 3B). As shown in Figure 3C and Table S1, the total energy change (ΔE) for the [^{99m}Tc]Tc-AuK-NapLPRO-HYNIC-EDDA labeling process was calculated to be 596.56 kcal/mol. The radiochemical purities (RCP) for [^{99m}Tc]Tc-AuK-LPRO-HYNIC-TPPTS/TPPMS/EDDA were 99.36%, 99.46%, and 93.43%, respectively. For [^{99m}Tc]Tc-AuK-DPRO-HYNIC-TPPTS/TPPMS/EDDA, the RCP were 98.14%, 99.23%, and 94.22%. In the case of [^{99m}Tc]Tc-AuK-NapLPRO-HYNIC-TPPTS/TPPMS/EDDA, RCP of 96.68%, 98.73%, and 95.01% were observed. Finally, [^{99m}Tc]Tc-AuK-NapDPRO-HYNIC-TPPTS/TPPMS/EDDA showed RCP of 98.31%, 96.92%, and 93.66%. All the radiotracers exhibited a RCP greater than 90% (Figure 4A-D) and could thus be directly used in subsequent studies without further purification.

Stability and Log *P* Assessment

As shown in Figure S1, all 12 radiotracers demonstrated stability in saline for up to 4 h. Notably, the four EDDA-based tracers—[^{99m}Tc]Tc-AuK-LPRO-HYNIC-EDDA, [^{99m}Tc]Tc-AuK-DPRO-HYNIC-EDDA, [^{99m}Tc]Tc-AuK-NapLPRO-HYNIC-EDDA, and [^{99m}Tc]Tc-AuK-NapDPRO-HYNIC-EDDA—also remained stable in fresh mouse whole blood over the same 4 h period. These results collectively confirm the good stability of all the labeled probes under *in vitro* physiological conditions. As revealed by DFT calculations, the highest occupied molecular orbital−lowest unoccupied molecular orbital (HOMO−LUMO) energy gap was 2.75 eV for the labeled complex [^{99m}Tc]Tc-AuK-NapLPRO-HYNIC-EDDA (Figure 3C), whereas the gaps for the individual reactants, AuK-NapLPRO-HYNIC and [^{99m}Tc]Tc-EDDA, were 6.82 and 5.45 eV, respectively. As shown in Figure 4E and Table S3, all the radiotracers were hydrophilic (Log *P* = −0.33 ∼−3.04). Among them, [^{99m}Tc]Tc-AuK-LPRO-HYNIC-TPPTS was the most hydrophilic (Log *P* = −3.04 ± 0.04), followed by [^{99m}Tc]Tc-AuK-NapLPRO-HYNIC-EDDA (Log *P* = −3.00 ± 0.03). In contrast, [^{99m}Tc]Tc-AuK-NapDPRO-HYNIC-TPPMS showed the greatest lipophilicity (Log *P* = −0.33 ± 0.08). Further comparison revealed that the coligands EDDA and TPPTS significantly enhanced tracer hydrophilicity, considerably outperforming TPPMS.

https://doi.org/10.1021/acs.jmedchem.5c03275
J. Med. Chem. XXXX, XXX, XXX−XXX

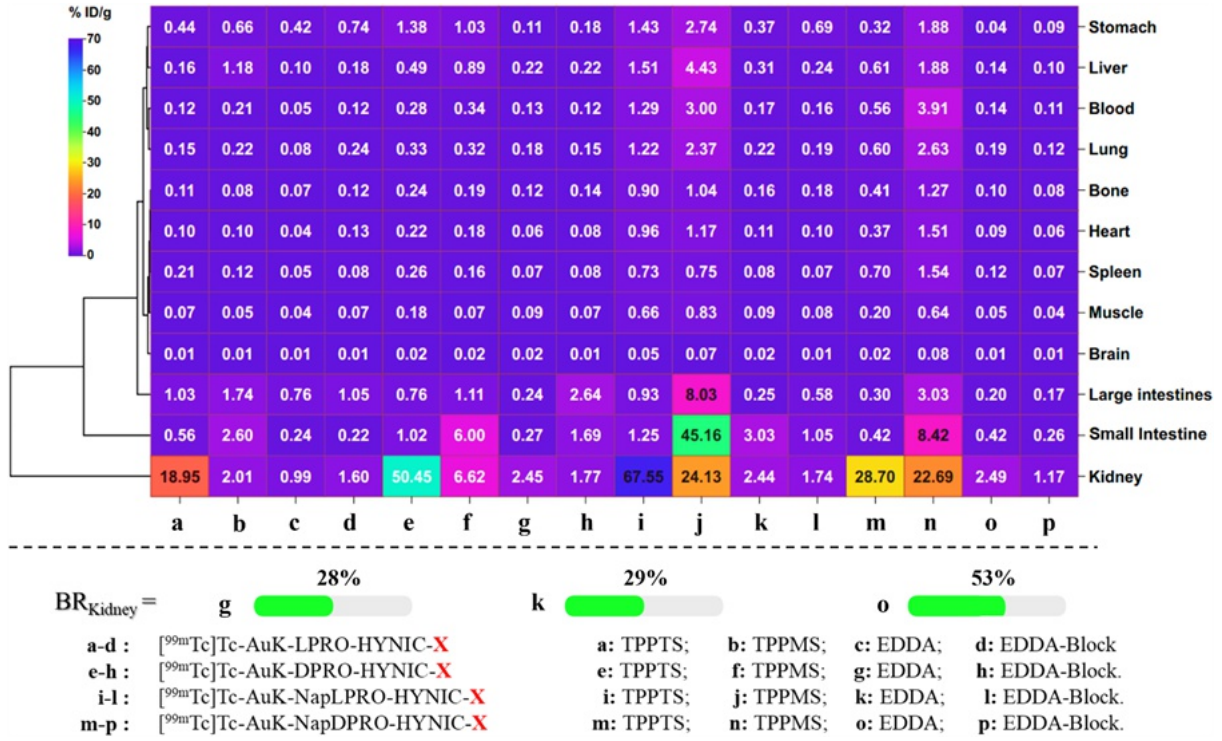

Figure 5. Biodistribution of radiotracers in normal Kunming mice (n = 5) at 2 h after injection.

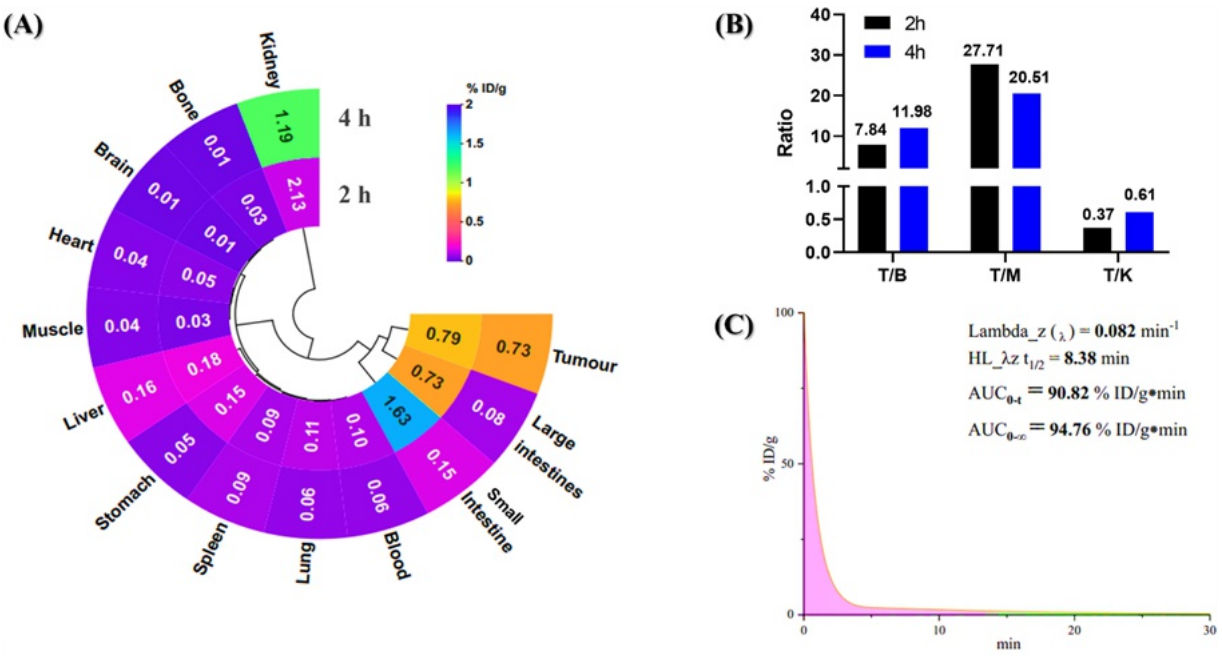

Figure 6. (A) [^{99m}Tc]Tc-AuK-NapLPRO-HYNIC-EDDA biodistribution in 22Rv1 tumor-bearing mice (n = 3) at 2 and 4 h after injection; (B) TBRs in biodistribution; and (C) Blood clearance of [^{99m}Tc]Tc-AuK-NapLPRO-HYNIC-EDDA in normal Kunming mice (n = 3) within 0−30 min.

Biodistribution Studies

Preliminary pharmacokinetic studies of all the radiotracers were performed in normal Kunming mice (Figure 5 and Tables S4−S7). Cluster analysis of the biodistribution revealed the greatest radiotracer accumulation in the kidneys (0.99 ∼ 67.55% ID/g, 2 h), followed by the intestines (0.20 ∼ 45.16% ID/g, 2 h). A comparison of the effects of different coligands indicated a consistent trend across the four labeled precursors. When EDDA was used as the coligand, clearance from nontarget organs was markedly more efficient than when TPPTS or TPPMS was used as a coligand, particularly clearance from the liver, spleen, lungs, and kidneys. EDDA-based tracers also exhibited rapid blood clearance (<1% ID/g, 2 h). In contrast, compared with TPPTS and EDDA, the use of TPPMS as a coligand led to significantly greater intestinal and blood uptake, a finding potentially attributable to the greater

https://doi.org/10.1021/acs.jmedchem.5c03275
J. Med. Chem. XXXX, XXX, XXX−XXX

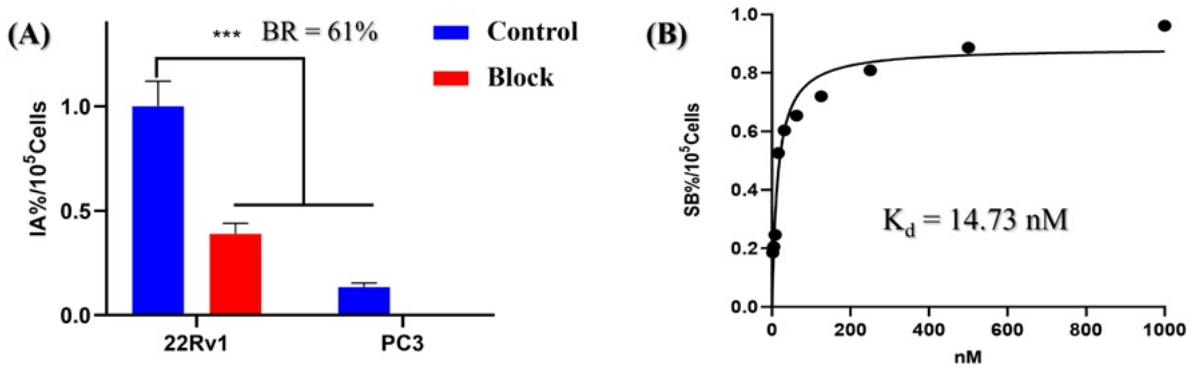

Figure 7. (A) Uptake of [^{99m}Tc]Tc-AuK-NapLPRO-HYNIC-EDDA in 22Rv1 (PSMA+) and PC3 (PSMA-) cells at 2 h; and (B) Saturation binding experiments of [^{99m}Tc]Tc-AuK-NapLPRO-HYNIC-EDDA in 22Rv1 cells. ***P < 0.001.

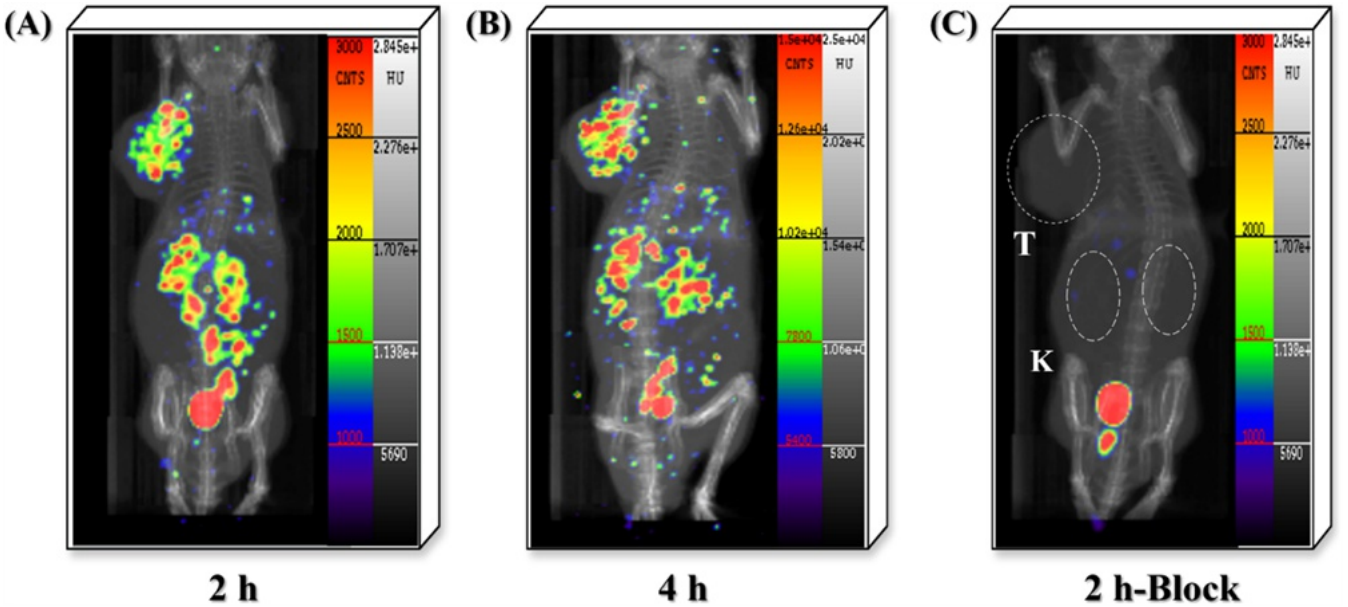

Figure 8. Micro-SPECT/CT images of [^{99m}Tc]Tc-AuK-NapLPRO-HYNIC-EDDA in 22Rv1 tumor-bearing male BALB/c nude mice at 2 and 4 h after injection.

lipophilicity of TPPMS. All four EDDA-based radiotracers exhibited the advantageous feature of low kidney uptake (<2.5% ID/g, 2 h). Specifically, the lowest kidney uptake was observed for [^{99m} Tc]Tc-AuK-LPRO-HYNIC-EDDA (0.99 ± 0.10% ID/g), followed by [^{99m}Tc]Tc-AuK-NapLPRO-HYNIC-EDDA (2.44 ± 0.33% ID/g), [^{99m}Tc]Tc-AuK-DPRO-HYNIC-EDDA (2.45 ± 0.15% ID/g), and [^{99m}Tc]Tc-AuK-NapDPRO-HYNIC-EDDA (2.49 ± 0.13% ID/g). In the 2-PMPA blocking study, the kidney blocking rates for [^{99m}Tc]Tc-AuK-DPRO-HYNIC-EDDA, [^{99m}Tc]Tc-AuK-NapLPRO-HYNIC-EDDA, and [^{99m}Tc]Tc-AuK-NapDPRO-HYNIC-EDDA were 28%, 29%, and 53%, respectively. Furthermore, all the radiotracers except those with TPPMS as a coligand demonstrated rapid clearance from blood, muscle, and bone (<1% ID/g, 2 h), with the four EDDA-based tracers showing particularly low background interference and considerable potential for improving the target-to-background ratios (TBRs).

The biodistribution of [^{99m}Tc]Tc-AuK-NapLPRO-HYNIC-EDDA in 22Rv1 tumor-bearing mice is shown in Figure 6A and Table S8. The kidney showed the greatest uptake (2.13 ± 0.73% ID/g, 2 h), followed by the intestines and tumor (1.63 ± 0.93% ID/g, 0.79 ± 0.09% ID/g, 2 h, respectively). Over time, the tracer continued to clear from nontargeted organs, particularly the kidneys (2.13 ± 0.73% ID/g, 2 h vs 1.19 ± 0.19% ID/g, 4 h). Moreover, tumor uptake was well retained (0.79 ± 0.09% ID/g, 2 h vs 0.73 ± 0.04% ID/g, 4 h). This rapid clearance profile contributed to high TBRs. The tumor-to-blood (T/B) and tumor-to-muscle (T/M) ratios were 7.84 and 27.71 at 2 h and 11.98 and 20.51 at 4 h, respectively. Notably, favorable tumor-to-kidney (T/K) ratios were also achieved, measuring 0.37 at 2 h and 0.61 at 4 h (Figure 6B). The PK properties of [^{99m}Tc]Tc-AuK-NapLPRO-HYNIC-EDDA in blood within 30 min are shown in Figure 6C and Table S9. The main PK parameters of Lambda_z (λ), HL_λz $t_{1/2}$ and $AUC_{0\text{-}t}$ were 0.082 min^{-1}, 8.38 min and 90.82%ID/g*min, respectively, and the theoretically predicted of $AUC_{0\text{-}\infty}$ were 94.76%ID/g*min.

Cellular Uptake Studies

The cellular uptake of [^{99m}Tc]Tc-AuK-NapLPRO-HYNIC-EDDA was evaluated in 22Rv1 (PSMA+) and PC3 (PSMA−) cell lines. As shown in Figure 7A, uptake was significantly greater in PSMA-positive 22Rv1 cells than in PSMA-negative PC3 cells. This uptake in 22Rv1 cells was effectively blocked by 2-PMPA, resulting in a blocking rate of 61%. Furthermore, the uptake in PC3 cells was only 14.7% of that observed in

https://doi.org/10.1021/acs.jmedchem.5c03275
J. Med. Chem. XXXX, XXX, XXX−XXX

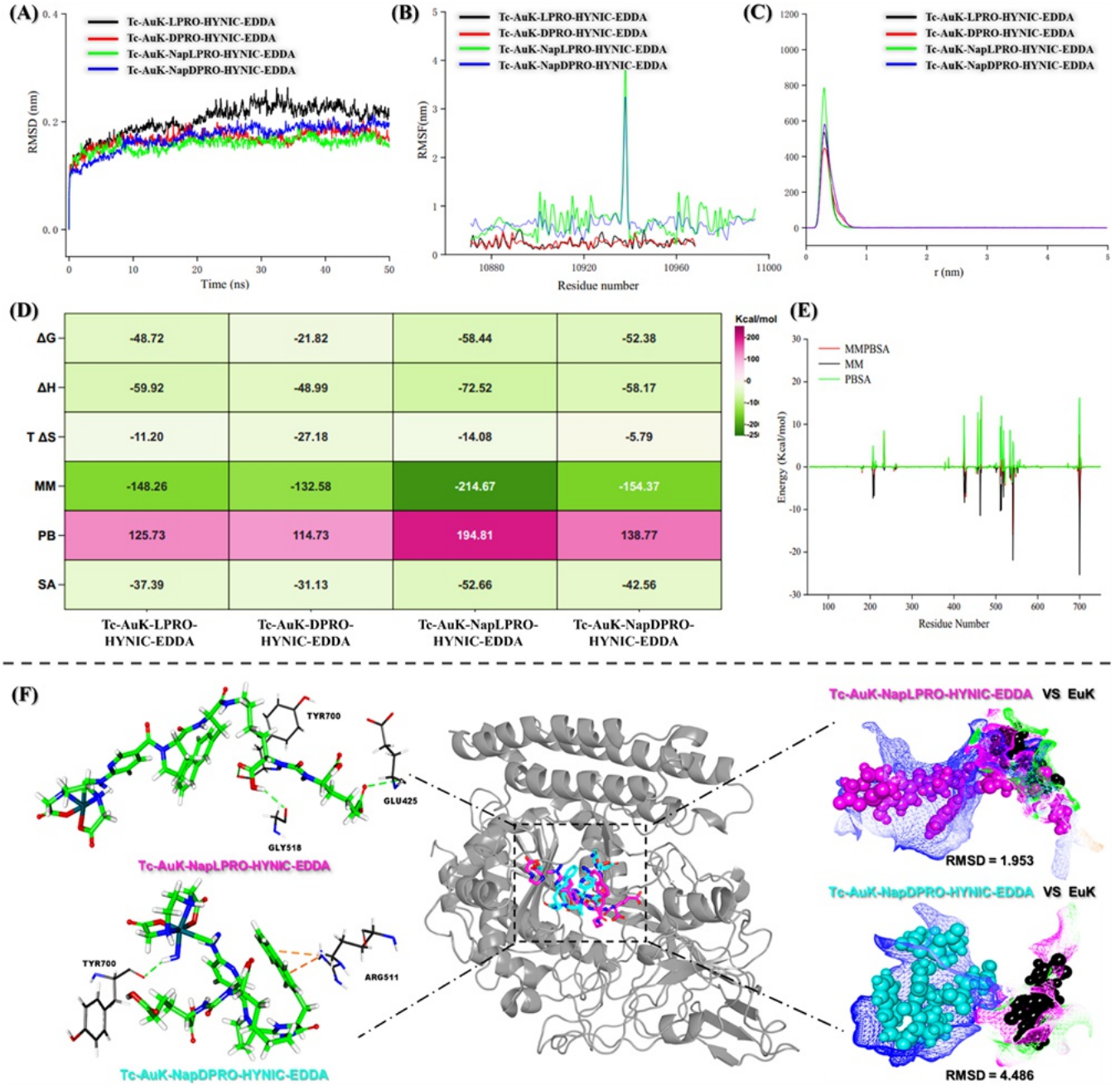

Figure 9. Molecular dynamics of radiotracers (PDB: 4LQG). (A) RMSD of the protein backbone; (B) RMSF of the ligands; (C) g(r) of the ligands; (D) MMPBSA energy decomposition; (E) Contribution of protein residues to the MMPBSA energy of Tc-AuK-NapLPRO-HYNIC-EDDA; and (F) Conformational comparison of Tc-AuK-NapLPRO-HYNIC-EDDA and Tc-AuK-NapDPRO-HYNIC-EDDA.

22Rv1 cells. Saturation binding experiments in 22Rv1 cells revealed that the dissociation constant (K_d) of the tracer for PSMA was 14.73 nM (Figure 7B).

Micro-SPECT/CT Imaging Studies

The imaging potential of EDDA as a coligand was evaluated in 22Rv1 tumor-bearing mice (Figures 8 and S2). SPECT/CT imaging revealed that all four EDDA-based tracers—[^{99m}Tc]-Tc-AuK-LPRO-HYNIC-EDDA, [^{99m}Tc]Tc-AuK-DPRO-HYNIC-EDDA, [^{99m}Tc]Tc-AuK-NapLPRO-HYNIC-EDDA, and [^{99m}Tc]Tc-AuK-NapDPRO-HYNIC-EDDA—could effectively localize tumors at 2 h postinjection, while distinct metabolic profiles were observed in the kidneys and other organs. Compared with [^{99m}Tc]Tc-AuK-DPRO-HYNIC-EDDA, [^{99m}Tc]Tc-AuK-LPRO-HYNIC-EDDA yielded a clearer background with negligible liver uptake, although its tumor accumulation was lower. The low accumulation of [^{99m}Tc]Tc-AuK-NapLPRO-HYNIC-EDDA in the kidneys and its high uptake within tumors indicate the most favorable potential for SPECT imaging, with both 2 and 4 h showing high-contrast SPECT images. The accumulation of [^{99m}Tc]Tc-AuK-NapDPRO-HYNIC-EDDA in tumors was not significant, and no considerable image contrast was obtained. In contrast, its renal uptake was significantly greater than that of [^{99m}Tc]Tc-AuK-NapLPRO-HYNIC-EDDA. Furthermore, pre-injection of 2-PMPA effectively blocked the uptake of [^{99m}Tc]Tc-AuK-NapLPRO-HYNIC-EDDA in both tumors and kidneys, confirming its ability to target PSMA specifically.

https://doi.org/10.1021/acs.jmedchem.5c03275
J. Med. Chem. XXXX, XXX, XXX−XXX

Molecular Dynamics Studies

The binding of four EDDA-based tracers with the PSMA protein was theoretically studied by molecular dynamics (MD). As shown in Figures 9A-F and S3, the root-mean-square deviation (RMSD) and root-mean-square fluctuation (RMSF) represent the formation of a stable protein−ligand complex, verifying the tight binding between the ligand and the protein. The radial distribution of the ligand confirms the presence of significant interactions within a range of 0.5 nm. MMPBSA binding energy calculations and decomposition analysis revealed that Tc-AuK-NapLPRO-HYNIC-EDDA had the most favorable protein affinity (ΔG = −58.44 kcal/mol), followed by Tc-AuK-NapDPRO-HYNIC-EDDA and Tc-AuK-LPRO-HYNIC-EDDA, while Tc-AuK-DPRO-HYNIC-EDDA had the lowest binding affinity (ΔG = −52.38 kcal/mol vs −48.72 kcal/mol vs −21.82 kcal/mol, respectively). Furthermore, compared with the other two tracers, both Tc-AuK-NapLPRO-HYNIC-EDDA and Tc-AuK-NapDPRO-HYNIC-EDDA demonstrated superior molecular mechanics (MM) energies (−214.67 and −154.37 kcal/mol, respectively) and nonpolar solvation (SA) energies (−52.66 and −42.56 kcal/mol, respectively). Analysis of protein−ligand interactions revealed that Tc-AuK-NapLPRO-HYNIC-EDDA forms multiple hydrogen bonds with key residues GLU425, GLY518, and TYR700 within the deep binding pocket. Molecular superposition with the reference compound EuK in the protein cavity (Figure 9F) revealed a significantly lower RMSD for Tc-AuK-NapLPRO-HYNIC-EDDA than Tc-AuK-NapDPRO-HYNIC-EDDA (1.953 vs 4.486), indicating a closer conformational match to EuK. Furthermore, within the binding pocket, the spatial overlap of Tc-AuK-NapLPRO-HYNIC-EDDA showed superior spatial overlap with EuK; additionally, the overlapping component was the pharmacophore (AuK) in the Tc-AuK-NapLPRO-HYNIC-EDDA molecule, a feature that is absent in Tc-AuK-NapDPRO-HYNIC-EDDA. Furthermore, MMPBSA energy decomposition of the Tc-AuK-NapLPRO-HYNIC-EDDA−protein complex identified GLU425, GLY518, and TYR700 as the key residues contributing most significantly to the binding energy, underscoring their crucial role in stabilizing the protein−ligand complex (Figure 9E).

DISCUSSION

EuK-derived PSMA-targeting radiotracers often exhibit high and persistent uptake in the kidneys and other normal organs in clinical applications, which has become a limitation of EuK-based tracers.[7] This is particularly concerning for therapeutic agents, as this uptake may lead to unavoidable toxic side effects.[31] Recent studies have suggested that the high uptake of EuK-based tracers in the kidneys and salivary glands may be attributed to the Glu moiety within the EuK pharmacophore.[15] Therefore, in this study, we chose to modify the targeting group using aminoadipic acid, aiming to positively influence the renal uptake profile of the tracer. The molecular docking results of the modified targeting group AuK revealed a distinct binding mode within the PSMA active cavity compared with that of the EuK molecule. AuK has a longer molecular topological distance (15.8 Å vs 10.9 Å), with the lysine moiety shifting toward the Zn^{2+} domain and disengaging from the S1 pocket, while the urea group moves closer to the P1' pocket. The aminoadipic acid chain extends outward, forming stable hydrogen bond interactions with residues GLU425, ARG463, ASN519, ARG534, and LYS545. Molecular docking scores indicate that the binding affinity potential of AuK is comparable to that of EuK (−10.00 kcal/mol vs −9.40 kcal/mol), validating the rationale for modifying the targeting group with aminoadipic acid. To further optimize the tracer, proline—which has the potential to reduce renal retention—was selected as the linker to investigate the effects of the two different configurations on the pharmacokinetic properties of the tracer. Additionally, the effects of the presence or absence of naphthylalanine on absolute tumor uptake were explored. Consequently, using AuK as the targeting group, 12 stable ^{99m}Tc-labeled PSMA tracers were designed and prepared by varying the type of linker between the targeting group and the chelator, as well as the composition of the coligand.

The ^{99m}Tc labeling method is straightforward, and the radionuclide is readily available. Twelve stable PSMA radiotracers can be used directly without purification (RCP > 90%), facilitating widespread promotion and clinical application. The coordination structure of the [^{99m}Tc]Tc-HYNIC labeling core remains unclear.[32] Structural optimization of [^{99m}Tc]Tc-AuK-NapLPRO-HYNIC-EDDA was performed using DFT, revealing distances of 11.7 Å, 10.1 Å, and 5.3 Å from the Tc metal center to the aminoadipic acid group, the aromatic ring center of naphthylalanine, and the aromatic ring center of the HYNIC chelator, respectively. The radiolabeling process requires a 20 min reaction at 100 °C. DFT calculations indicated a total energy change (ΔE) of 596.56 kcal/mol for the reaction, suggesting that the formation of stable [^{99m}Tc]Tc-AuK-NapLPRO-HYNIC-EDDA requires the absorption of 596.56 kcal/mol of heat. This represents the first calculation of the labeling reaction energy for [^{99m}Tc]Tc-HYNIC-EDDA-based tracers and provides valuable theoretical insights for optimizing the labeling conditions of such tracers.

The 12 radiotracers demonstrated stability in saline for 4 h, and four tracers with EDDA as the coligand maintained the same 4 h stability in fresh mouse whole blood. These results collectively confirm the favorable stability of all labeled tracers under *in vitro* physiological conditions. DFT molecular orbital energy gap calculations revealed that the energy gap of [^{99m}Tc]Tc-AuK-NapLPRO-HYNIC-EDDA was 2.75 eV, whereas the energy gaps of the reactants AuK-NapLPRO-HYNIC and [^{99m}Tc]Tc-EDDA were 6.82 and 5.45 eV, respectively. The molecular orbital energy gap is a key indicator of chemical reactivity, and a larger energy gap (>2 eV) increases the difficulty of electron transition from occupied to unoccupied orbitals,[33] further validating the high stability of both the labeling process and the final labeled product. All the radiotracers exhibited hydrophilic characteristics (Log P = −0.33 ∼ −3.04). Among them, [^{99m}Tc]Tc-AuK-LPRO-HYNIC-TPPTS was the most hydrophilic (Log P = − 3.04 ± 0.04), followed by [^{99m}Tc]Tc-AuK-NapLPRO-HYNIC-EDDA (Log P = − 3.00 ± 0.03). By modulating the composition of different coligands, it was observed that EDDA and TPPTS significantly improved the hydrophilicity of the tracers, markedly outperforming the coligand TPPMS. With the exception of AuK-LPRO-HYNIC, the combinations of the other three labeling precursors with the coligand EDDA exhibited a superior hydrophilic trend compared with that of TPPTS.

A preliminary evaluation of the pharmacokinetic properties of all radiotracers was conducted in normal Kunming mice to identify lead tracers for further investigation. When the effects of different coligands on the biodistribution of the radiotracers were compared, the four labeling precursors exhibited

https://doi.org/10.1021/acs.jmedchem.5c03275
J. Med. Chem. XXXX, XXX, XXX−XXX

consistent trends. With EDDA as the coligand, clearance from nontarget organs was significantly better than with TPPTS and TPPMS, particularly in the liver, spleen, lungs, and kidneys, while faster clearance rates from the blood were also demonstrated. Compared with those with TPPTS and EDDA, the four tracers with TPPMS as the coligand showed notably greater uptake in the intestines, which may be attributed to their greater lipophilicity. When TPPTS served as the coligand, the tracers exhibited significantly greater metabolism in the kidneys, possibly related to the metabolic pathway of TPPTS. Renal uptake serves as an important reference indicator for radiotracer screening. Among the four radiotracers with EDDA as the coligand, all demonstrated the advantage of low kidney uptake (<2.5% ID/g, 2 h). The L-proline linker demonstrated superior efficacy over the D-proline linker in reducing kidney uptake (0.99 ± 0.10% ID/g vs 2.45 ± 0.15% ID/g) in precursors without the naphthylalanine linker. However, upon incorporation of the naphthylalanine linker, no significant difference in kidney uptake (2.44 ± 0.33% ID/g vs 2.49 ± 0.13% ID/g) was observed between the two configurations. As the kidney is a high PSMA-expressing organ,[34] the kidneys showed blocking rates of 28%, 29%, and 53% for [^{99m}Tc]Tc-AuK-DPRO-HYNIC-EDDA, [^{99m}Tc]Tc-AuK-NapLPRO-HYNIC-EDDA, and [^{99m}Tc]Tc-AuK-NapDPRO-HYNIC-EDDA, respectively, upon 2-PMPA blockade, demonstrating the good PSMA targeting specificity of these compounds. Owing to its efficient kidney clearance (<2% ID/g), [^{99m}Tc]Tc-AuK-LPRO-HYNIC-EDDA did not exhibit significant blocking effects, which may be attributed to its low baseline uptake in kidneys. A similar phenomenon was observed for our previous PSMA-targeting tracers: [^{99m}Tc]Tc-EUKD-EDDA also resulted in favorable kidney clearance (1.58 ± 0.06% ID/g) in Kunming mice, and no obvious blocking was observed after 2-PMPA preinjection.[18] Furthermore, all the radiotracers were rapidly cleared from the blood, muscle, and bone (<1% ID/g, 2 h). In particular, the four tracers with EDDA as the coligand demonstrated lower background interference and significant potential for improving TBRs, thus qualifying as lead tracers for subsequent SPECT/CT imaging studies.

The SPECT/CT imaging potential of four EDDA-based coligand tracers was evaluated in 22Rv1 tumor-bearing mice, with performance assessed via SPECT/CT images at 2 h postinjection. All four tracers effectively identified tumor lesions, though variations in their metabolism were observed in the kidneys and other organs ([^{99m}Tc]Tc-AuK-NapDPRO-HYNIC-EDDA were due to the exposure being adjusted to a unified standard for lateral comparison with similar tracers, resulting in its uptake not being prominent in tumors). Compared with [^{99m}Tc]Tc-AuK-DPRO-HYNIC-EDDA, [^{99m}Tc]Tc-AuK-LPRO-HYNIC-EDDA exhibited a clearer background without significant liver uptake, although its tumor accumulation appeared slightly lower. [^{99m}Tc]Tc-AuK-NapLPRO-HYNIC-EDDA demonstrated significantly greater tumor uptake along with the advantage of low renal retention when compared to [^{99m}Tc]Tc-AuK-NapDPRO-HYNIC-EDDA. Cross-comparison revealed that [^{99m}Tc]Tc-AuK-NapLPRO-HYNIC-EDDA offers a distinct advantage in enhancing tumor uptake while reducing renal retention—a result highly consistent with our initial optimization strategy. A comparison between [^{99m}Tc]Tc-AuK-NapLPRO-HYNIC-EDDA and [^{99m}Tc]Tc-AuK-LPRO-HYNIC-EDDA revealed that the introduction of naphthylalanine significantly increased tumor accumulation. In terms of linker configuration, tracers incorporating L-proline ([^{99m}Tc]Tc-AuK-LPRO-HYNIC-EDDA and [^{99m}Tc]Tc-AuK-NapLPRO-HYNIC-EDDA) demonstrated superior reductions in nontarget organ uptake compared with their D-proline counterparts ([^{99m}Tc]Tc-AuK-DPRO-HYNIC-EDDA and [^{99m}Tc]Tc-AuK-NapDPRO-HYNIC-EDDA), which is consistent with the biodistribution patterns observed in Kunming mice. Furthermore, preadministration of 2-PMPA effectively blocked the uptake of [^{99m}Tc]-Tc-AuK-NapLPRO-HYNIC-EDDA in both tumors and kidneys, confirming its specific targeting capability toward PSMA. High-contrast SPECT/CT images of [^{99m}Tc]Tc-AuK-NapLPRO-HYNIC-EDDA were obtained at both 2 and 4 h postinjection. Therefore, this tracer demonstrates substantial potential for clinical application, supporting both standard scanning and time-lapse imaging protocols.

The biodistribution of [^{99m}Tc]Tc-AuK-NapLPRO-HYNIC-EDDA was investigated in 22Rv1 tumor-bearing mouse models. At 2 h postinjection, consistent with observations in Kunming mice, the kidneys exhibited the greatest uptake (2.13 ± 0.73% ID/g), followed by the intestines and tumors (1.63 ± 0.93% ID/g and 0.79 ± 0.09% ID/g, respectively). Compared with our previously studied PSMA probe [^{99m}Tc]Tc-T-M2 (which uses EuK as the targeting moiety), kidney uptake was reduced by more than 30-fold (72.66 ± 4.40% ID/g vs 2.13 ± 0.73% ID/g, 2 h).[35] Over time, the tracer continued to clear from nontarget organs, particularly from the kidneys (2.13 ± 0.73% ID/g, 2 h vs 1.19 ± 0.19% ID/g, 4 h). Moreover, tumor uptake remained well preserved (0.79 ± 0.09% ID/g, 2 h vs 0.73 ± 0.04% ID/g, 4 h). This rapid clearance profile significantly improved the TBRs. The T/B and T/M ratios reached 7.84 and 27.71 at 2 h and 11.98 and 20.51 at 4 h, respectively. Notably, the *T*/K ratio was also effectively enhanced, with values of 0.37 and 0.61 measured at 2 and 4 h, respectively. Although the absolute tumor uptake shows promise, it is still lower than that of clinically successful tracers. Consequently, enhancing the tracer's affinity and refining its pharmacokinetics constitute the principal objectives for future optimization. The short retention time (HL_λz $t_{1/2}$ = 8.38 min), rapid clearance rate (Lambda_z (λ) = 0.082 min^{-1}) and lower blood-time effective area ($AUC_{0\text{-}t}$ = 90.82%ID/g*min) of [^{99m}Tc]Tc-AuK-NapLPRO-HYNIC-EDDA in the bloodstream provide a strong foundation for achieving high TBRs. The primary objective of this study—to reduce absolute kidney uptake and improve TBRs, especially the *T*/K ratio, by modifying the targeting group—was confirmed as a rational design strategy, as supported by the biodistribution results in 22Rv1 tumor-bearing mice.

Differences in the cellular uptake of [^{99m}Tc]Tc-AuK-NapLPRO-HYNIC-EDDA were compared between 22Rv1 (PSMA+) and PC3 (PSMA-) cells. The uptake of [^{99m}Tc]Tc-AuK-NapLPRO-HYNIC-EDDA in 22Rv1 cells was 85.3% greater than that in PC3 cells. This uptake in 22Rv1 cells could be effectively blocked by 2-PMPA, with a blocking rate of 61%. The differential uptake between 22Rv1 and PC3 cells, along with the effective blocking, demonstrates the favorable PSMA-targeting ability of [^{99m}Tc]Tc-AuK-NapLPRO-HYNIC-EDDA. Furthermore, the affinity of [^{99m}Tc]Tc-AuK-NapLPRO-HYNIC-EDDA for PSMA was measured through saturation binding assays in 22Rv1 cells (K_d = 14.73 nM), which further confirmed the high binding affinity of the tracer for PSMA protein. The binding of the tracers to PSMA protein was theoretically investigated using MD. MMPBSA energy

https://doi.org/10.1021/acs.jmedchem.5c03275
J. Med. Chem. XXXX, XXX, XXX−XXX

calculations and decomposition revealed that Tc-AuK-NapLPRO-HYNIC-EDDA has the most favorable protein binding affinity (ΔG = −58.44 kcal/mol). Tc-AuK-NapLPRO-HYNIC-EDDA demonstrated significant advantages in MM (−214.67 kcal/mol) and SA (−52.66 kcal/mol), indicating more favorable interactions and desolvation effects within the active cavity of the protein. Analysis of ligand−protein interactions revealed that it forms extensive hydrogen bonds with GLU425, GLY518, and TYR700 deep within the binding pocket. MMPBSA energy decomposition of the Tc-AuK-NapLPRO-HYNIC-EDDA protein−ligand complex further revealed GLU425, GLY518, and TYR700 as key residues contributing substantially to the binding energy, highlighting their crucial role in maintaining protein−ligand stability. Using Tc-AuK-NapLPRO-HYNIC-EDDA and Tc-AuK-NapDPRO-HYNIC-EDDA as representative examples, the impact of the proline configuration on performance was examined. MMPBSA calculations indicated that the binding characteristics of Tc-AuK-NapLPRO-HYNIC-EDDA are superior to those of Tc-AuK-NapDPRO-HYNIC-EDDA (−58.44 kcal/mol vs −52.38 kcal/mol), primarily due to energy differences in MM (−214.67 kcal/mol vs −154.37 kcal/mol) and SA (−52.66 kcal/mol vs −42.56 kcal/mol), suggesting that Tc-AuK-NapLPRO-HYNIC-EDDA achieves more favorable protein−ligand interactions and hydrophobic pocket compatibility. Molecular alignment comparison with the positive control molecule EuK within the protein binding cavity revealed that Tc-AuK-NapLPRO-HYNIC-EDDA results in less conformational deviation and better spatial overlap with EuK. The overlapping region corresponds precisely to the pharmacophore (AuK) within the Tc-AuK-NapLPRO-HYNIC-EDDA structure—a feature not observed in Tc-AuK-NapDPRO-HYNIC-EDDA. Structural analysis revealed that compared with its Tc-AuK-NapDPRO-HYNIC-EDDA counterpart, Tc-AuK-NapLPRO-HYNIC-EDDA penetrates deeper into the active pocket of PSMA protein, which likely accounts for its high protein affinity. Theoretical investigation of the binding affinity between four EDDA-based tracers and the PSMA protein through MD demonstrated that Tc-AuK-NapLPRO-HYNIC-EDDA possesses the most favorable protein binding profile, which aligns with the trends observed in both *in vitro* and *in vivo* activity evaluations. It should be noted, however, that tracer performance is influenced by multiple factors, with protein binding affinity being among the critical determinants. These findings provide valuable insights into the binding mechanism of Tc-AuK-NapLPRO-HYNIC-EDDA to PSMA protein.

CONCLUSIONS

In this study, we designed and synthesized four novel precursors for radiolabeling to target PSMA and successfully prepared 12 stable radiotracers by combining ^{99m}Tc with different coligands. All the tracers demonstrated favorable stability and underwent preliminary pharmacokinetic evaluation. Among them, [^{99m}Tc]Tc-AuK-NapLPRO-HYNIC-EDDA exhibited the most promising imaging potential. It binds stably within the active cavity of PSMA protein, displaying nanomolar affinity (K_d = 14.73 nM), and shows significant tumor uptake both in cellular assays and on SPECT imaging. Its targeting specificity toward PSMA was further confirmed by effective blocking in both *in vitro* and *in vivo* experiments. The coordination structure of tracers is rationalized through DFT, which establishes the theoretical framework, while MD are employed to unravel the molecular-level details of ligand-protein binding. [^{99m}Tc]Tc-AuK-NapLPRO-HYNIC-EDDA effectively reduced absolute uptake in the kidneys and resulted in good tumor retention, and its rapid clearance from nontarget organs resulted in high TBRs. More importantly, this tracer enabled the acquisition of high-contrast SPECT/CT images within 2−4 h postinjection, offering distinct advantages for time-lapse imaging. This characteristic is crucial for enhancing the clinical diagnostic accuracy of prostate cancer. In summary, [^{99m}Tc]Tc-AuK-NapLPRO-HYNIC-EDDA represents a promising candidate for the development of PSMA-targeted tumor imaging agents.

EXPERIMENTAL SECTION

General

All chemical reagents were sourced from Tong Guang Fine Chemicals Company (Beijing, China), Aladdin, Innochem, and J&K. ^{1}H NMR spectra were acquired on a JNM-ECS spectrometer (JEOL, Tokyo, Japan) operating at 400 or 600 MHz. Mass spectrometry (MS) data were collected using a Thermo Scientific LCQ mass spectrometer equipped with an electrospray ionization (ESI) source. The purity of all the precursors was greater than 95%. Radioactive high-performance liquid chromatography (R-HPLC) analyses were performed on a Shimadzu 20A system (Shimadzu, Kyoto, Japan) equipped with a Kromasil C18 column (250 × 4.6 mm, 5 μm). [^{99m}Tc]$NaTcO_4$ was eluted from a ^{99} Mo/^{99m}Tc generator (Zhibo Bio-Medical Technology, Beijing, China) using saline. Radioactivity was quantified using a Wizard 2480 γ-counter (PerkinElmer, Singapore). The 22Rv1 and PC3 cell lines were provided by the Typical Culture Collection of the Chinese Academy of Sciences (Beijing, China). *In vivo* imaging was conducted on a micro-SPECT/CT system (Trifoil, CA). MD and DFT calculations were carried out on a high-performance computing system configured with a 44-core/88-thread CPU, 128 GB of RAM, and an RTX 2080 Ti GPU (22 GB) under the Ubuntu 22.04.2 operating system.

Radiolabeling

[^{99m}Tc]Tc-AuK-LPRO-HYNIC-TPPTS. Tricine (1 mg) and TPPTS (2 mg) were dissolved in 0.5 mL of phosphate-buffered saline (PBS). To this mixture, succinate buffer adjusted to a pH of 6.0 was added (0.3 mL), followed by AuK-LPRO-HYNIC (10 μg) and 0.5 mL of freshly eluted [^{99m}Tc]$NaTcO_4$ (37−370 MBq) in sequence, and the mixture was then subjected to a reaction at 100 °C for 30 min to yield the radiotracer [^{99m}Tc]Tc-AuK-LPRO-HYNIC-TPPTS.

[^{99m}Tc]Tc-AuK-LPRO-HYNIC-TPPMS. Tricine (1 mg) and TPPMS (2 mg) were dissolved in 0.5 mL of PBS. To this mixture, succinate buffer adjusted to a pH of 6.0 was added (0.3 mL), followed by AuK-LPRO-HYNIC (10 μg) and 0.5 mL of freshly eluted [^{99m}Tc]$NaTcO_4$ (37−370 MBq) in sequence, and the mixture was then subjected to a reaction at 100 °C for 30 min to yield the radiotracer [^{99m}Tc]Tc-AuK-LPRO-HYNIC-TPPMS.

[^{99m}Tc]Tc-AuK-LPRO-HYNIC-EDDA. Tricine (20 mg) and EDDA (10 mg) were dissolved in 0.5 mL of PBS. To this solution, succinate buffer adjusted to a pH of 7.0 was added (0.2 mL), the solution pH was adjusted to 7.0−8.0 with NaOH (1 mol/L), followed by AuK-LPRO-HYNIC (10 μg), $SnCl_2\ 2H_2O$ (100 μg) and 0.5 mL of freshly eluted [^{99m}Tc]$NaTcO_4$ (37−370 MBq) in sequence, and the mixture was then subjected to a reaction at 100 °C for 20 min to yield the radiotracer [^{99m}Tc]Tc-AuK-LPRO-HYNIC-EDDA.

The preparation methods for the other three labeled precursor tracers are identical to that of AuK-LPRO-HYNIC, except that the corresponding labeled precursors need to be substituted.

R-HPLC Analysis and Stability Assay

The RCP and *in vitro* stability of the ^{99m}Tc-labeled radiotracers were analyzed by R-HPLC using a Shimadzu 20A system equipped with a Kromasil C18 column (250 × 4.6 mm, 5 μm). The mobile phase consisted of water containing 0.1% trifluoroacetic acid (TFA) as

https://doi.org/10.1021/acs.jmedchem.5c03275
J. Med. Chem. XXXX, XXX, XXX−XXX

phase A and acetonitrile as phase B. The injection volume was 10 μL, and the flow rate was maintained at 1.0 mL/min. The gradient elution program was set as follows: 10% B (0−2 min), increased linearly from 10% to 90% B (2−5 min), held at 90% B (5−20 min), and then returned linearly to 10% B (20−25 min).

The *in vitro* stability of the radiotracers was evaluated in both saline and mouse whole blood. To assess whole-blood stability, the radiotracers were mixed with fresh mouse blood at a 1:1 (v/v) ratio and incubated at 37 °C for 4 h. Subsequently, a 1:2 mixture of acetonitrile and ethanol was added to precipitate plasma proteins. The sample was then centrifuged at 12,000 rpm for 5 min at 4 °C, and the resulting supernatant was passed through a 0.22-μm membrane filter before R-HPLC analysis to determine the RCP. Parallel stability testing in saline was conducted by incubating the radiolabeled solution at 37 °C for 4 h, followed by direct R-HPLC measurement of RCP.

Octanol/Water Partition Coefficient (Log *P*)

The Log *P* values of the radiotracers were determined using the shake flask method. Prior to the experiment, the *n*-octanol was presaturated by equilibrating it overnight with PBS (0.025 mol/L, pH 7.4). Briefly, 900 μL of PBS, 1 mL of presaturated *n*-octanol, and 100 μL of radiotracer were combined in a centrifuge tube and vigorously shaken for 5 min. The mixture was then centrifuged at 10000 rpm for 15 min to achieve phase separation. Subsequently, 500 μL aliquots from both the PBS and *n*-octanol phases were collected, and their radioactivity was measured using a γ-counter. The distribution coefficient was calculated on the basis of the radiocounts in each phase and is expressed as Log *P* = log (cpm in *n*-octanol/cpm in PBS). The results were derived from three independent parallel experiments and are presented as the mean ± SD.

Cell Culture and Tumor Models

The 22Rv1 (PSMA+) and PC3 (PSMA-) cancer cell lines were cultured in RPMI 1640 media supplemented with 10% (v/v) heat-inactivated fetal bovine serum (FBS) and 1% (v/v) penicillin streptomycin at 37 °C in a cell culture incubator with 5% CO_2.

All mice were obtained from Shibeifu Experimental Animal Company (Beijing, China). Male Kunming mice (4−5 weeks old) were used for preliminary pharmacokinetic studies. For biodistribution and SPECT imaging, male BALB/c nude mice (4−5 weeks) were inoculated subcutaneously in the flank with 100 μL of a 22Rv1 cell suspension (~1×10^7 cells) to generate tumor-bearing models. These experiments were performed 3 weeks later, when the tumors had grown to 5−12 mm in diameter.

All animals were raised in a pathogen-free 26 °C environment with ample space for movement, socialization, and natural behaviors. They had continuous access to clean water and a balanced feed. All of the animal protocols were approved and supervised by the Institutional Animal Care and Use Committee of Beijing Normal University (permit no. BNUCC-EAW-2022001).

Biodistribution Studies in Mice

In the preliminary pharmacokinetic study of all the radiotracers, Kunming mice (n = 5) were utilized for evaluation. Each mouse was administered a ^{99m}Tc-labeled tracer (1.85 ± 0.05 MBq in 100 μL) via tail vein injection and euthanized 2 h postinjection. Blood and major organs—including the heart, liver, spleen, lungs, kidneys, muscle, bone, stomach, brain, large intestine, and small intestine—were collected, weighed, and measured for radioactivity using a γ-counter. A biodistribution study was conducted using the 22Rv1 tumor-bearing mouse model (n = 3) following the same experimental procedure. In the blocking study, a group of mice was preinjected with the PSMA-selective inhibitor 2-PMPA (500 μg in 100 μL) 30 min prior to radiotracer administration. All mice subsequently received an intravenous injection of the ^{99m}Tc-labeled tracer (1.85 ± 0.05 MBq/100 μL). The animals were euthanized at 2 h postinjection. The biodistribution results are expressed as the percentage of injected dose per gram of tissue (%ID/g) and are presented as the mean ± SD. Additionally, blood samples were collected from Kunming mice at 0, 5, 15, and 30 min after tracer administration, and their radioactivity was quantified with a γ-counter. Pharmacokinetic parameters were derived by fitting a noncompartmental model to the blood radioactivity−time profile using Phoenix software.

Cellular Uptake and Saturation Binding Assay *In Vitro*

22Rv1 and PC3 cells were seeded in 24-well plates (1×10^5 cells per well) and incubated overnight. Each well was then treated with 0.5 mL of fresh culture medium containing [^{99m}Tc]Tc-AuK-NapLPRO-HYNIC-EDDA (0.37 MBq). After 2 h of incubation, the medium was aspirated, and the cells were washed twice with cold PBS. The cells were subsequently lysed using 1 M NaOH. Radioactivity in the lysates was quantified using a γ-counter. In the blocking experiment, the experimental group workflow was followed after the PSMA inhibitor 2-PMPA (1 μM) was used for intervention 30 min prior. The data are presented as the means ± SDs, and the results are expressed as the percentage of injected activity (IA %)/10^5 cells relative to the 22Rv1 control group.

The affinity of [^{99m}Tc]Tc-AuK-NapLPRO-HYNIC-EDDA for PSMA was determined via a saturation binding assay in 22Rv1 cells. Cells seeded in 96-well plates were incubated with increasing concentrations of the radiotracer (1.56−1000 nM). To assess binding specificity, a separate inhibition group was pretreated with a high dose of the competitor (500 nM/well) for 30 min prior to the addition of the radiotracer. After 1 h of incubation, the medium was aspirated, and the cells were washed twice with cold PBS. The cells were subsequently lysed with 1 M NaOH, and the cell-associated radioactivity was measured using a γ-counter. The results are expressed as the percentage of specific binding per 10^5 cells (%SB/10^5 cells). The dissociation constant (K_d) was calculated from the resulting data using GraphPad Prism 8.2.

Micro-SPECT/CT Imaging

Radiotracers (37 MBq, 100 μL) were intravenously administered to 22Rv1 tumor-bearing mice. Prior to imaging, the mice were anesthetized with 3% (v/v) isoflurane. SPECT/CT scans were obtained at 2 and 4 h postinjection under maintenance anesthesia with 1.5% isoflurane delivered in the air at a flow rate of 500 mL/min. Blocking studies were conducted in 22Rv1 tumor-bearing mice. Mice in the experimental group received an intravenous injection of the PSMA-specific inhibitor 2-PMPA (500 μg) 30 min prior to the administration of the ^{99m}Tc-labeled radiotracer (37 MBq in 100 μL). SPECT images were acquired at 2 h after injection of the radiotracer. All the images were reconstructed and analyzed using Vivo Quant 2.4 software.

DFT Calculations

DFT calculations were carried out using Gaussian 16. All calculations employed the M062X functional and dgdzvp basis set. The HOMO and LUMO energy levels were obtained using Gaussian 16. Geometry optimizations and frequency calculations of AuK-NapLPRO-HYNIC, [^{99m}Tc]Tc-EDDA and [^{99m}Tc]Tc-AuK-NapLPRO-HYNIC-EDDA were performed at the M062X functional and dgdzvp basis set levels. Finally, the obtained molecular orbitals were rendered using Gauss View software.

Molecular Docking and Dynamics Assay

Molecular docking was performed using AutoDock 4.2. The crystal structure of the target protein (PDB: 4LQG) was obtained from the Protein Data Bank (PDB) and prepared as the receptor. The small-molecule ligand was geometrically optimized in Gaussian 16 prior to docking. The docking site was defined around the cocrystallized ligand, and default parameters were used throughout the procedure. The resulting docking pose was further subjected to MD simulation using Gromacs 2020. The protein was described with the Amber 99SB force field, while ligand parameters were derived from GAFF. The system was solvated in an SPC water model and neutralized. After energy minimization, stepwise equilibration was performed under NVT and NPT ensembles for 2 ns each, followed by a 50 ns MD production run. The trajectory was analyzed in terms of RMSD, RMSF, and g(r). The last 10 ns of the trajectory was used for the

https://doi.org/10.1021/acs.jmedchem.5c03275
J. Med. Chem. XXXX, XXX, XXX−XXX

MMPBSA free energy calculations and per-residue energy decomposition. Visualization of the final simulated conformation was carried out using PyMOL.

■ ASSOCIATED CONTENT

Supporting Information

The Supporting Information is available free of charge at https://pubs.acs.org/doi/10.1021/acs.jmedchem.5c03275.

Molecular formula strings (CSV)

Synthesis of precursor, Supporting Information for radiotracer stability and Log *P*, Supporting Information for biodistribution, micro-SPECT/CT imaging, molecular dynamics, DFT calculations, ^{1}H NMR, MS and HPLC spectra (PDF)

■ AUTHOR INFORMATION

Corresponding Authors

Junbo Zhang − *Key Laboratory of Radiopharmaceuticals of the Ministry of Education, College of Chemistry, NMPA Key Laboratory for Research and Evaluation of Radiopharmaceuticals (National Medical Products Administration), Beijing Normal University, Beijing 100875, P. R. China;* orcid.org/0000-0003-3549-6483; Email: zhjunbo@bnu.edu.cn

Jianyong Jiang − *Key Laboratory of Beam Technology of the Ministry of Education, College of Physics and Astronomy, Beijing Normal University, Beijing 100875, P. R. China;* Email: jianyong@bnu.edu.cn

Authors

Zuojie Li − *Key Laboratory of Radiopharmaceuticals of the Ministry of Education, College of Chemistry, NMPA Key Laboratory for Research and Evaluation of Radiopharmaceuticals (National Medical Products Administration) and Key Laboratory of Beam Technology of the Ministry of Education, College of Physics and Astronomy, Beijing Normal University, Beijing 100875, P. R. China;* orcid.org/0009-0001-1131-1635

Peiwen Han − *Key Laboratory of Radiopharmaceuticals of the Ministry of Education, College of Chemistry, NMPA Key Laboratory for Research and Evaluation of Radiopharmaceuticals (National Medical Products Administration), Beijing Normal University, Beijing 100875, P. R. China*

Lina Diao − *Key Laboratory of Radiopharmaceuticals of the Ministry of Education, College of Chemistry, NMPA Key Laboratory for Research and Evaluation of Radiopharmaceuticals (National Medical Products Administration), Beijing Normal University, Beijing 100875, P. R. China*

Complete contact information is available at: https://pubs.acs.org/10.1021/acs.jmedchem.5c03275

Notes

The authors declare no competing financial interest.

■ ACKNOWLEDGMENTS

This work was financially supported, in part, by the National Natural Science Foundation of China (22476011, 22276015), the Beijing Natural Science Foundation (2232010) and the Beijing Nova Program (20230484470).

■ ABBREVIATIONS

DFT, Density functional theory; EDDA, ethylenediaminediacetic acid; HATU, 2-(7-azabenzotriazol-1-yl)-*N*,*N*,*N*′,*N*′-tetramethyluronium hexafluorophosphate; HOMO, highest occupied molecular orbital; HYNIC, hydrazinonicotinamide; LUMO, lowest unoccupied molecular orbital; MD, Molecular dynamics; MM, molecular mechanics energy; MMPBSA, molecular mechanicspoisson-boltzmann surface area; MS, mass spectra; NMR, nuclear magnetic resonance; PB, polar solvation energy; PBS, phosphate buffered saline; PDB, protein data bank; PSMA, prostate-specific membrane antigen; RCP, radiochemical purity; R-HPLC, radioactive high-performance liquid chromatography; RMSD, root-mean-square deviation; RMSF, root-mean-square fluctuation; SA, nonpolar solvation energy; SPECT, single photon emission computed tomography; TBRs, tumor-to-background ratios; TPPTS, triphenylphosphine trisulfonate; TPPMS, diphenylphosphine benzene-3-sulfonate; ΔS, entropy

■ REFERENCES

(1) Siegel, R. L.; Giaquinto, A. N.; Jemal, A. Cancer Statistics, 2024. *CA Cancer J. Clin.* **2024**, *74* (1), 12−49.

(2) Sung, H.; Ferlay, J.; Siegel, R. L.; Laversanne, M.; Soerjomataram, I.; Jemal, A.; Bray, F. Global Cancer Statistics 2020: Globocan Estimates of Incidence and Mortality Worldwide for 36 Cancers in 185 Countries. *CA Cancer J. Clin.* **2021**, *71* (3), 209−249.

(3) Sallam, M.; Nguyen, N.-T.; Sainsbury, F.; Kimizuka, N.; Muyldermans, S.; Benešová-Schäfer, M. PSMA-Targeted Radiotheranostics in Modern Nuclear Medicine: Then, Now, and What of the Future? *Theranostics* **2024**, *14* (8), 3043−3079.

(4) Filippi, L.; Frantellizzi, V.; Chiaravalloti, A.; Pontico, M.; De Feo, M. S.; Corica, F.; Montebello, M.; Schillaci, O.; De Vincentis, G.; Bagni, O. Prognostic and Theranostic Applications of Positron Emission Tomography for a Personalized Approach to Metastatic Castration-Resistant Prostate Cancer. *Int. J. Mol. Sci.* **2021**, *22* (6), 3036−3061.

(5) Li, Z.; Ruan, Q.; Jiang, Y.; Wang, Q.; Yin, G.; Feng, J.; Zhang, J. Current Status and Perspectives of Novel Radiopharmaceuticals with Heterologous Dual-Targeted Functions: 2013−2023. *J. Med. Chem.* **2024**, *67* (24), 21644−21670.

(6) Lindsley, C. W.; Müller, C. E.; Bongarzone, S. Diagnostic and Therapeutic Radiopharmaceuticals: A "Hot" Topic. *J. Med. Chem.* **2023**, *66* (24), 16457−16463.

(7) Uijen, M. J. M.; Derks, Y. H. W.; Merkx, R. I. J.; Schilham, M. G. M.; Roosen, J.; Privé, B. M.; van Lith, S. A. M.; van Herpen, C. M. L.; Gotthardt, M.; Heskamp, S.; et al. PSMA Radioligand Therapy for Solid Tumors Other Than Prostate Cancer: Background, Opportunities, Challenges, and First Clinical Reports. *Eur. J. Nucl. Med. Mol. Imaging* **2021**, *48* (13), 4350−4368.

(8) Zhang, S.; Wang, X.; Gao, X.; Chen, X.; Li, L.; Li, G.; Liu, C.; Miao, Y.; Wang, R.; Hu, K. Radiopharmaceuticals and Their Applications in Medicine. *Signal Transduction Target Ther.* **2025**, *10* (1), 1−46.

(9) Donin, N. M.; Reiter, R. E. Why Targeting PSMA Is a Game Changer in the Management of Prostate Cancer. *J. Nucl. Med.* **2018**, *59* (2), 177−182.

(10) Sathianathen, N. J.; Konety, B. R.; Crook, J.; Saad, F.; Lawrentschuk, N. Landmarks in Prostate Cancer. *Nat. Rev. Urol.* **2018**, *15* (10), 627−642.

(11) Rajasekaran, A. K.; Anilkumar, G.; Christiansen, J. J. Is Prostate-Specific Membrane Antigen a Multifunctional Protein? *Am. J. Physiol Cell Physiol.* **2005**, *288* (5), C975−C981.

(12) Kozikowski, A. P.; Zhang, J.; Nan, F.; Petukhov, P. A.; Grajkowska, E.; Wroblewski, J. T.; Yamamoto, T.; Bzdega, T.; Wroblewska, B.; Neale, J. H. Synthesis of Urea-Based Inhibitors as

Active Site Probes of Glutamate Carboxypeptidase II: Efficacy as Analgesic Agents. *J. Med. Chem.* **2004**, *47* (7), 1729−1738.
(13) Kozikowski, A. P.; Nan, F.; Conti, P.; Zhang, J.; Ramadan, E.; Bzdega, T.; Wroblewska, B.; Neale, J. H.; Pshenichkin, S.; Wroblewski, J. T. Design of Remarkably Simple, yet Potent Urea-Based Inhibitors of Glutamate Carboxypeptidase II (Naaladase). *J. Med. Chem.* **2001**, *44* (3), 298−301.
(14) Lawhn-Heath, C.; Salavati, A.; Behr, S. C.; Rowe, S. P.; Calais, J.; Fendler, W. P.; Eiber, M.; Emmett, L.; Hofman, M. S.; Hope, T. A. Prostate-Specific Membrane Antigen PET in Prostate Cancer. *Radiology* **2021**, *299* (2), 248−260.
(15) Kuo, H.-T.; Lin, K.-S.; Zhang, Z.; Zhang, C.; Merkens, H.; Tan, R.; Roxin, A.; Uribe, C. F.; Bénard, F. What a Difference a Methylene Makes: Replacing Glu with Asp or Aad in the Lys-Urea-Glu Pharmacophore of PSMA-Targeting Radioligands to Reduce Kidney and Salivary Gland Uptake. *Theranostics* **2022**, *12* (14), 6179−6188.
(16) Chen, Y.; Foss, C. A.; Byun, Y.; Nimmagadda, S.; Pullambhatla, M.; Fox, J. J.; Castanares, M.; Lupold, S. E.; Babich, J. W.; Mease, R. C.; Pomper, M. G. Radiohalogenated Prostate-Specific Membrane Antigen (PSMA)-Based Ureas as Imaging Agents for Prostate Cancer. *J. Med. Chem.* **2008**, *51* (24), 7933−7943.
(17) Wang, X.; Chen, Y.; Xiong, Y.; Zhang, L.; Wang, B.; Liu, Y.; Cui, M. Design and Characterization of Squaramic Acid-Based Prostate-Specific Membrane Antigen Inhibitors for Prostate Cancer. *J. Med. Chem.* **2023**, *66* (10), 6889−6904.
(18) Li, Z.; Duan, X.; Han, P.; Yin, G.; Jiang, Y.; Ruan, Q.; Zhang, J. Synthesis and Evaluation of ^{99m}Tc-Labeled L-Aspartic Acid as a Euk Polymer Linker for Targeting PSMA to a Novel SPECT Tumor Tracer. *J. Med. Chem.* **2024**, *67* (23), 21617−21628.
(19) Li, Z.; Jiang, Y.; Ruan, Q.; Yin, G.; Han, P.; Duan, X.; Zhang, J. Synthesis and Evaluation of ^{99m}Tc-Labeled $_D$Pro-Gly-Containing Tracers Targeting PSMA. *Mol. Pharm.* **2024**, *21* (10), 5305−5314.
(20) Duan, X.; Liu, F.; Kwon, H.; Byun, Y.; Minn, I.; Cai, X.; Zhang, J.; Pomper, M. G.; Yang, Z.; Xi, Z.; et al. (S)-3-(Carboxyformamido)-2-(3-(Carboxymethyl)Ureido)Propanoic Acid as a Novel PSMA Targeting Scaffold for Prostate Cancer Imaging. *J. Med. Chem.* **2020**, *63* (7), 3563−3576.
(21) Ren, Y. N.; Liu, C.; Liu, T.; Duan, X.; Zhang, Q.; Liu, J.; Wang, P.; Guo, Q.; Yang, X.; Du, P.; et al. Preclinical Evaluation and First in Human Study of Al^{18}F Radiolabeled Odap-Urea-Based PSMA Targeting Ligand for PET Imaging of Prostate Cancer. *Front. Oncol.* **2022**, *12*, 1030187.
(22) Duan, X.; Cao, Z.; Zhu, H.; Liu, C.; Zhang, X.; Zhang, J.; Ren, Y. N.; Liu, F.; Cai, X.; Guo, X.; et al. ^{68}Ga-Labeled Odap-Urea-Based PSMA Agents in Prostate Cancer: First-in-Human Imaging of an Optimized Agent. *Eur. J. Nucl. Med. Mol. Imaging* **2022**, *49* (3), 1030−1040.
(23) Lu, K.; Zhang, C.; Zhang, Z.; Kuo, H.-T.; Colpo, N.; Bénard, F.; Lin, K.-S. Synthesis and Evaluation of ^{99m}Tc-Labeled PSMA-Targeted Tracers Based on the Lys-Urea-Aad Pharmacophore for Detecting Prostate Cancer with Single Photon Emission Computed Tomography. *Molecules* **2023**, *28* (13−24), 5120−5131.
(24) Kubyshkin, V.; Rubini, M. Proline Analogues. *Chem. Rev.* **2024**, *124* (13), 8130−8232.
(25) Kubyshkin, V.; Mykhailiuk, P. K. Proline Analogues in Drug Design: Current Trends and Future Prospects. *J. Med. Chem.* **2024**, *67* (22), 20022−20055.
(26) Feng, J.; Wang, Q.; Yin, G.; Jiang, Y.; Ruan, Q.; Han, P.; Xiao, Q.; Ding, D.; Li, Z.; Du, J.; et al. Synthesis and Preclinical Evaluation of Novel ^{99m}Tc-Labeled FR-Targeting Agents with Satisfactory Imaging Contrast and Reduced Renal Uptake. *J. Med. Chem.* **2025**, *68* (5), 5675−5686.
(27) Li, Z.; Diao, L.; Han, P.; Xiao, Q.; Ding, D.; Feng, J.; Jiang, J.; Zhang, J. D. Synthesis, and Evaluation of a Novel ^{99m}Tc-Labeled Small Molecule Inhibitor (Lapatinib)-Based SPECT Tracer Targeting HER2. *J. Med. Chem.* **2025**, *68* (21), 23620−23631.
(28) Martina Benešová, M. S.; Bauder-Wüst, U.; Afshar-Oromieh, A.; Kratochwil, C.; Mier, W.; Haberkorn, U.; Kopka, K.; Eder, M. Preclinical Evaluation of a Tailor-Made DOTA-Conjugated PSMA Inhibitor with Optimized Linker Moiety for Imaging and Endoradiotherapy of Prostate Cancer. *J. Nucl. Med.* **2015**, *56* (6), 914−920.
(29) Brunello, S.; Salvarese, N.; Carpanese, D.; Gobbi, C.; Melendez-Alafort, L.; Bolzati, C. A Review on the Current State and Future Perspectives of [^{99m}Tc]Tc-Housed PSMA-i in Prostate Cancer. *Molecules* **2022**, *27* (9), 2617−2656.
(30) Shi, J.; Liu, S. Clinical Application of ^{99m}Tc-Labeled Peptides for Tumor Imaging: Current Status and Future Directions. *iRadiology* **2024**, *2* (1), 17−34.
(31) Farolfi, A.; Calderoni, L.; Mattana, F.; Mei, R.; Telo, S.; Fanti, S.; Castellucci, P. Current and Emerging Clinical Applications of PSMA PET Diagnostic Imaging for Prostate Cancer. *J. Nucl. Med.* **2021**, *62* (5), 596−604.
(32) Duatti, A. Review on ^{99m}Tc Radiopharmaceuticals with Emphasis on New Advancements. *Nucl. Med. Biol.* **2021**, *92*, 202−216.
(33) Truhlar, D. A.-O.; Hiberty, P. A.-O.; Shaik, S. A.-O.; Gordon, M. A.-O. X.; Danovich, D. A.-O. Orbitals and the Interpretation of Photoelectron Spectroscopy and (E,2e) Ionization Experiments. *Angew. Chem., Int. Ed.* **2019**, *58*, 12332−12338.
(34) Neels, O. C.; Kopka, K.; Liolios, C.; Afshar-Oromieh, A. Radiolabeled PSMA Inhibitors. *Cancers* **2021**, *13* (24), 6255−6278.
(35) Xiao, D.; Han, P. W.; Jiang, Y. H.; Duan, X. J.; Ruan, Q.; Zhang, Z. B.; Chen, X. L.; Zhang, J. B. Preparation, Biological Evaluation, and First-in-Human Single-Photon Emission Computed Tomography (SPECT) Study of ^{99m}Tc-Labeled Prostate-Specific Membrane Antigen (PSMA)-Targeted Radiotracers Containing Triazole with Reduced Kidneys Accumulation. *ACS Pharmacol. Transl. Sci.* **2024**, *7* (5), 1335−1347.

https://doi.org/10.1021/acs.jmedchem.5c03275
J. Med. Chem. XXXX, XXX, XXX−XXX